Asia-Pacific Journal of Science and Technology: Volume: 30. Issue: 03. Article ID.: APST-30-03-05. Research Article

APST

Asia-Pacific Journal of Science and Technology

https://www.tci-thaijo.org/index.php/APST/index

Published by Research Department,
Khon Kaen University, Thailand

The surrogate assisted design optimization of a twisted oval tube heat exchanger

Pitak Promthaisong[1], Bopit Bubphachot[1], Teerapat Chompookham[1], Narin Siriwan[1] and Kittinan Wansasueb[1, *]

[1]Heat Pipe and Thermal Equipment Design Research Unit, Department of Mechanical Engineering, Faculty of Engineering, Mahasarakham University, 44150
[*]Corresponding author: kittinan.w@msu.ac.th

Received 20 February 2024
Revised 11 September 2024
Accepted 26 September 2024

Abstract

A design for a twisted oval tube (TOT) heat exchanger using a surrogate-assisted metaheuristic (MH) optimization technique is proposed in this work. The heat transfer characteristic in the TOTs is presented using the computational fluid dynamic (CFD) method, considering parameters such as pitch ratios (PR), cross-sectional ratios (DR), and Reynolds number (*Re*) ranging from 0.6 to 1.4, 0.02 to 0.1, and 100 to 2,000, respectively. The fitness functions were considered as multi-objective, including the Nusselt number (*Nu*) and the Poiseuille number (*fRe*) [1]. To reduce the time consumed in the design procedure, surrogate-assisted optimization was applied in the optimum design search phase. Well-known surrogate models (SuMo), including the Kriging (KRG), radial basis function interpolation (RBF), and k-nearest neighborhood method (KNN), were investigated and compared when applied with metaheuristic algorithms. The results show that the most acceptable prediction model is the RBF-Inverse Multiquadric kernel with the multi-objective meta-heuristic with iterative parameter distribution estimation (MMIPDE), with average errors of 20.9731 and 15.6011 for *Nu* and *fRe*, respectively.

Keywords: Twisted oval tube, Heat transfer, Surrogate model, Kriging, Surrogate-assisted design optimization

1. Introduction

Heat exchangers are utilized in various industries, including the petroleum, chemical, food, power plant, and food processing industries for processes such as heat treatment for control of bacteria. To improve overall thermal efficiency and heat transfer rates, heat exchangers can be improved through various techniques, such as passive heat transfer enhancement methods that do not require external energy input. The passive method involves modification of the internal flow structure of heat exchanger tubes using devices, also called turbulators or vortex generators [2], for example baffles [3, 4], fins [2, 5, 6], twisted tapes [7–10], grooved [11] and roughened surfaces [12] etc. Among the various techniques of the passivation method, using a tube with a rough surface is most commonly employed to enhance heat transfer rates [13, 14]. This is achieved by inducing a swirling flow pattern and increasing the mixing of the fluid between the center and near-wall regions of the tube. As a result, the heat transfer rate at the tube wall is significantly increased.

Numerous researchers have conducted studies on improving heat transfer rates in heat exchangers through various techniques, including modifications to the internal flow structure. Among these techniques, the use of heat exchanger tubes with roughened surfaces such as ribbed tubes, micro-finned tubes, helically grooved tubes [11], and twisted tubes have been investigated extensively in the field of heat transfer enhancement. For example, Naphon and Wiriyasart [15] studied the effect of micro-finned tubes on laminar pulsating flow and heat transfer with magnetic fields. They reported that the micro-finned tubes provided superior heat transfer compared with smooth tubes. Jianfeng et al. [16] reported turbulent convective heat transfer in a spirally grooved tube. They found that the spirally grooved tubes gave heat transfer higher than that of smooth tubes due to the effect of the spiral groove. Increasing the groove height can increase the heat transfer. Razzaghi et al. [17] reported the thermo-hydraulic performance evaluation of a twisted flat tube in turbulent flow. They found that the twisted flat tube provided thermo-hydraulic performance 70% higher than the smooth tube. Promthaisong et al. [18] investigated the effect of twisting ratio of the twisted square duct for heat transfer enhancement. They found that the maximum thermal enhancement factor of 1.42 was at the twist ratio of 3.5. In the range studied, the heat transfer was found to be in the range 31 - 52%. Recently in 2023, Eiamsa-ard et al. [19] investigated ribbed twisted-oval tubes for heat transfer enhancement, and found that the ribbed twisted-oval tubes provided higher heat transfer than that of both twisted-oval tubes and smooth circular tubes alone. Moreover, studies on nanofluid flow have been conducted since the early 2000s [9, 20–22]. Both numerical [9] and experimental [21] approaches have been used, and improvements have been made in optimization methods [20, 22].

The initial computational study on the subject of fluid dynamics and heat transfer was conducted in 1970 [23], while a calculation procedure for heat, mass and momentum transfer in three-dimensional parabolic flows was conducted in 1972 [24]. These numerical studies have been widely popular and disseminated compared to the earlier work, as they can help reduce experimental and computational resources [3]. In the context of heat exchanger optimization research, the typical design objectives are centered around the heat transfer performance and pressure loss. The evaluation of these objective functions traditionally involves the use of computational fluid dynamics (CFD) simulations, which are notorious for their time-consuming nature. Considering this challenge, surrogate-assisted optimization has been proposed as a means of addressing the optimization of heat exchangers [3]. For example, an oscillating fluid's effect on the temperature distribution throughout the pipe was predicted using the surrogate model, and could be extended to an optimum design in future works [25]. High-temperature polymer electrolyte membrane fuel cells (HT-PEMFCs) were designed by machine learning-based optimization [26]. The design of fixed-type packed bed reactors for chemical heat storage was conducted using a hyperparameter optimization framework technique called Optuna, coupling with evolutionary multi-objective optimization algorithms such as nondominated sorting genetic algorithm II (NSGA-II) [1, 27], Finally, Fawaz et al. [28] presented a literature review on the topology optimization of heat exchangers. The trend of heat exchanger design is focused on high heat transfer performance. The focus of the study was on conjugate heat transfer in heat exchangers. Topology optimization was applied.

As mentioned in the literature review above, direct optimization methods consume a significant amount of computing time. Reducing computational time is necessary. Therefore, the aim of this paper is to investigate the application of surrogate models with metaheuristic optimization for designing the twisted oval tube heat exchanger. The mathematical model of conjugate heat transfer and the surrogate model are detailed in Section 2. The numerical experiment setup, including objective function definition and parameter settings, is defined in Section 3. The results and discussion are detailed in Section 4, and the conclusion is presented in the final section.

2. Materials and methods

2.1 Conjugate heat transfer data reduction

This study investigates a twisted oval tube with a reference diameter (D), in which a surface tube is twisted with a length controlled by the twist length (p), representing the length of the twist over 360 degrees. The study explored various pitch ratios (PR, p/D) and cross-sectional ratios (DR, a/b) ranging from 0.6 to 1.4 and 0.02 to 0.1, respectively. Figure 1 provides a detailed illustration of the geometry. The numerical computation used air as the working fluid at a pressure of one atmosphere and a temperature of 300 K (Pr = 0.707) and computed with Reynolds numbers (*Re*) ranging from 100 to 2,000. The wall of the test section was assumed to be in a no-slip condition and a constant temperature of 310 K. The inlet and outlet were applied with the periodic condition [3, 7, 8, 10, 18, 29–31].

In this paper, the flow is described by three equations: continuity, Navier-Stokes equations, and the energy equation. These equations were developed under the following assumptions:

- The flow is three-dimensional, steady, laminar and incompressible.
- The fluid properties are constant.
- Body forces and viscous dissipation are negligible.
- Radiation heat transfer can be ignored.

Based on these assumptions, the governing equations in the Cartesian tensor system can be expressed as:

$$\textit{Continuity equation:} \frac{\partial (u_i)}{\partial x_i} = 0 \tag{1}$$

$$\textit{Momentum equation:} \frac{\partial (u_i u_j)}{\partial x_j} = -\frac{\partial P}{\partial x_i} + \frac{\partial}{\partial x_j}\left[\mu\left(\frac{\partial u_i}{\partial x_j} + \frac{\partial u_j}{\partial x_i}\right)\right] \tag{2}$$

$$\textit{Energy equation:} \frac{\partial}{\partial x_i}\left(u_j T\right) = \frac{\partial}{\partial x_j}\left(\Gamma \frac{\partial T}{\partial x_j}\right) \tag{3}$$

were Γ is the thermal diffusivity and is defined as: $\Gamma = \frac{\mu}{Pr}$

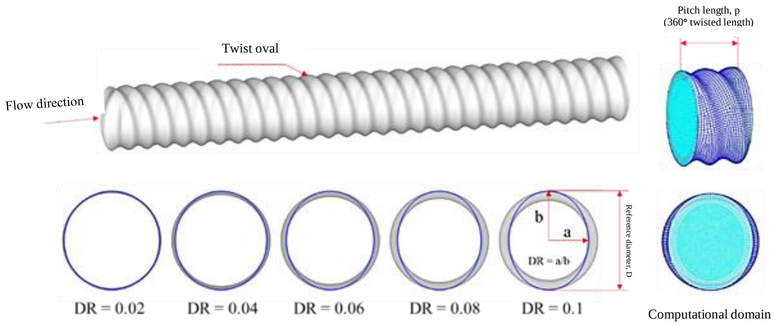

Figure 1 The schematic diagram of twisted oval tube.

The quadratic upstream interpolation for convective kinetics differencing scheme (QUICK) was used to discretize the energy equation, while the governing equations were discretized by the second-order upwind differencing scheme and decoupled with the semi–implicit method for pressure–linked equations algorithm (SIMPLE). The finite volume method was employed as a solver, following Patankar's method [23, 24]. Convergence was considered achieved when the normal residual values for all equations were less than 10^{-5}, except for the energy equation, which was set to less than 10^{-9}

The parameters of interest for the numerical method are Reynolds number, friction factor, average Nusselt number and the thermal enhancement factor, which are expressed in Equations (4), (5), (6), and Equation (7), respectively.

The Reynolds number was defined as

$$Re = \frac{\rho u D_h}{\mu} \tag{4}$$

while the friction factor, f, was calculated from the pressure drop (ΔP) along the length of the flow tube using the equation

$$f = 2(-\frac{dP}{dx})(\frac{D_h}{\rho u^2}) \tag{5}$$

The average Nusslet number can be calculated from

$$Nu = \frac{1}{A}\int Nu_x dA \tag{6}$$

The thermal enhancement factor (TEF), a performance indicator that accounts for both heat transfer and pressure loss under equal pumping power, can be expressed as:

$$TEF = (\frac{Nu}{Nu_0})/(\frac{f}{f_0})^{1/3} \tag{7}$$

where Nu_0 and f_0 are the Nusselt number and friction factor for a straight smooth circular tube, respectively.

2.2 Surrogate model

In the field of engineering, when it is difficult to measure or compute an outcome of interest, a surrogate model is used as a prediction method to evaluate the correlation between input and outcome. Well-known models in engineering design include the Kriging model (KRG) [32, 33], radial basis function interpolation (RBF) [34], support vector machine (SVM), polynomial response surface (PRS) [3], and k-nearest neighborhood method (KNN) [35]. Detailed information on the surrogate models is provided in the following sections.

2.2.1 Kriging model

KRG, also called Gaussian process regression, is a predictive technique using Wiener–Kolmogorov prediction developed by Norbert Wiener and Andrey Kolmogorov in 1960 [33]. This model has been continuously developed over time, and several popular models have used meta-heuristic algorithms to estimate the model's matrix coefficients, a process known as parameter estimation via meta-heuristics for Kriging [36, 37]. The equation for this model is presented below.

$$\hat{y} = \mu + \emptyset^T (\mathbf{U} \backslash (\mathbf{U^T} \backslash y - \{1\} \times \mu)) \tag{8}$$

where

$\emptyset = \exp(-\sum_{i=1}^{n} (\theta \times abs(\mathbf{x}_i - \mathbf{x})^{1.99}))$

$\mu = \frac{\{1\} \times \mathbf{U}(\mathbf{U^T} \backslash y)}{\{1\} \times \mathbf{U}(\mathbf{U^T} \backslash \{1\})}$

$\theta = 10^{\vartheta}$

where $\mathbf{U}$ and ϑ can be estimated by the hybrid grey wolf-adaptive differential evolution (GWADE) [37].

2.2.2 Radial basis function interpolation

Radial basis function (RBF) interpolation is a commonly used method in engineering design, similar to the Kriging model. The RBF model can also modify its kernel function by using various function types based on the governing equation [34], following:

$$\hat{y} = \sum_{i=1}^{n} \alpha_i K(\|\mathbf{x} - \mathbf{x}_i\|) \tag{9}$$

where α_i is a predicted coefficient matric

$\|\mathbf{x} - \mathbf{x}_i\|$ is an absolute radial distance of input parameter

K is a kernel function

where the kernel functions are detailed in the literature [38–42].

2.2.3 K-nearest neighbor method

KNN serves as the final competitor. KNN is a prediction technique based on the average value of the training set using input design vectors and their distances [35], as shown in Equation (10).

$$D_i = \sum (\mathbf{x}_i - \mathbf{x})^2 \tag{10}$$

Then the outcome can be predicted from the average value of the training set with the distance input design vector

$$\hat{y} = mean(\{y_k\})$$

were $\{y_k\}$ represents the outcome parameter population from the training points, and k is the population size of the training inputs. Generally, the total size of k can be set manually, with the maximum number being the total size of the training inputs.

In the present study, all the surrogate models mentioned above were employed to predict the twisted oval tube heat exchanger tube's design, and their performances were compared. The design training set and validation set were computed by the finite volume method [23, 24] and formed into groups by the k-means clustering method [43, 44]. To solve the problem, several multi-objective evolutionary algorithms (MOEAs) were employed, namely multi-objective meta-heuristic with iterative parameter distribution estimation (MMIPDE) [45], hybrid real-code population-based incremental learning and differential evolution (RPBILDE) [46], multi-objective cuckoo Search (MOCS) [47]. multi-objective grey wolf optimizer (MOGWO) [48] and non-dominated sorting genetic algorithm II (NSGA-II) [49]

2.3 Laboratory testing

All the tests were performed at the DPWH-accredited materials testing laboratory and in accordance with international standards. These include Los Angeles abrasion, sieve analysis, hygroscopic moisture content, density, liquid and plastic limits, compaction, CBR, and UCS.

3. Numerical experiment setup

This study is a comparison of metaheuristic (MH) optimization algorithms. The design vector ($\mathbf{x}_i$) is constructed by the cross-sectional ratios (DR), PR, and Re, respectively. Negligible inequality and equality constraints were present, while the design variable was bound-constrained. The objective function of this work was set as a multi-objective optimization problem. The investigation aimed to simultaneously optimize the Poiseuille number (fRe), and Nusselt number values, which present two conflicting goals [1]. To achieve this, a multi-objective optimization problem was formulated considering the design variables of *Re*, DR and PR following:

$$Maximize: f_1(\mathbf{x}) = Nu \qquad (11)$$
$$Minimize: f_2(\mathbf{x}) = fRe$$
$$subject\ to: \quad \mathbf{x}_l \leq \mathbf{x}_i \leq \mathbf{x}_u$$

It is important to mention that the relationship between the friction factor (f) and the *Re* does not behave in the same way as that of the pressure drop (ΔP). In fact, an increase in *Re* can cause a decrease in the f, but an increase in ΔP, illustrating a non-similar pattern between the two variables [1]. All the objective functions were predicted by the surrogate models above, while the k-mean clustering is applied for selecting the training points and validating points. The parameter setting of the competitive surrogate model is detailed in Table 1.

Table 1 The surrogate model parameter setup.

Surrogate model	Parameter name	Values or method
Kriging model (KRG)	model's matrix coefficients **U** and ϑ algorithm solver	hybrid grey wolf-adaptive differential evolution (GWADE)
Radial basis function (RBF)	kernel functions	Linear spline :$K = \lVert\mathbf{x} - \mathbf{x}_i\rVert$ Cubic spline :$K = \lVert\mathbf{x} - \mathbf{x}_i\rVert^3$ Gaussian technique: $K = exp(\varepsilon \times \lVert\mathbf{x} - \mathbf{x}_i\rVert) : \varepsilon = 1e-5$ Multiquadric technique: $K = sqrt(1 + (\varepsilon \times \lVert\mathbf{x} - \mathbf{x}_i\rVert^2)) : \varepsilon = 1e-5$ Inverse Quadric technique: $K = \frac{1}{1+(\varepsilon\times\lVert\mathbf{x}-\mathbf{x}_i\rVert^2)} : \varepsilon = 1e-5$ Inverse Multiquadric technique: $K = \frac{1}{sqrt(1+(\varepsilon\times\lVert\mathbf{x}-\mathbf{x}_i\rVert^2))} : \varepsilon = 1e-5$
K-nearest neighbor method (KNN)	population size of training inputs (k)	{2, 3, 5, 10}

The optimization procedure used in this study is called a MH. Five recent metaheuristic algorithms were utilized to construct the surrogate-assisted optimization approach for the TOT heat exchanger. The setup of optimization parameters is outlined in Table 2. The total number of function evaluations (FEs) is set to 20,000 FEs, and the population size is 50. The performance of the metaheuristic algorithms was evaluated using the hypervolume indicator [50] with the statistical tests including average (Mean), standard deviation (Std), maximum (Max) and minimum values (Min).

Table 2 The optimization parameter set up.

Algorithm	Parameter	Values
MMIPDE	First scaling factor (F_1)	[0.75,1.5]
	Second scaling factor ($F2$)	[0.1, 0.5]
	Crossover parameter (C_R)	[0.75, 1.0]
RPBILDE	Learning rate (L_R)	0.25
	Mutation probability (μ_{prop})	0.05
	Mutation shift (μ_{shift})	0.20
	Crossover probability	0.7
	Scaling factor for differential evolution (DE) operator (F)	0.8
	Probability of choosing Element from offspring in crossover (C_R)	0.5
MOCS	The Levy exponent in Levy flights (β)	1.5
MOGWO	Grid Inflation Parameter (α)	0.1
	Leader Selection Pressure Parameter (β)	4
	Extra Repository Member Selection Pressure (γ)	2
	Number of Grids per each Dimension (N_{grid})	10
NSGA-II	Mutation probability (P_m)	0.1

4. Results and discussion

4.1 Grid independence test

The smooth tube was used to validate by comparing with the exact solution found in the open literature [51]. The heat transfer (Nu) and f were reported as shown in Figure 2. In the figure, under a similar operating condition, the Nu and f of the smooth tube by the numerical method were found to be in excellent agreement with the exact solution with deviations less than 0.5%. The results indicate that the numerical method provides strong confidence in further studies of the heat transfer and friction factor in the twisted oval tube in the laminar flow region.

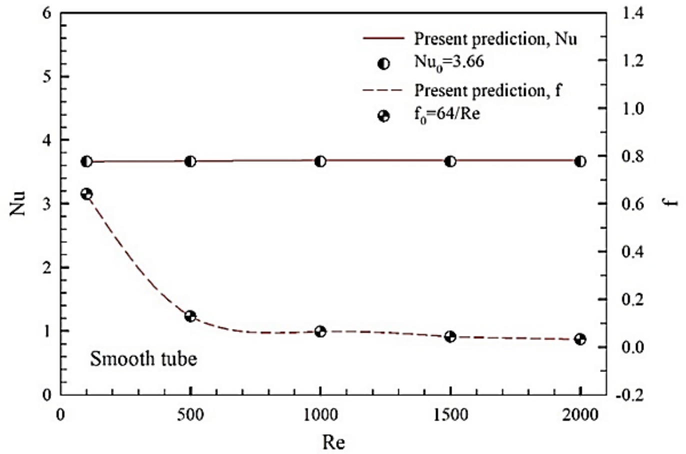

Figure 2 Verification for the smooth tube.

The grid number for the test section (using the TOT with PR=1.0 and DR=0.06) was used at around 80,000 elements, because a rise in the grid number from 80,000 to 100,000 changed the Nusselt number and friction factor by less than 0.5%, while a rise of the grid number from 40,000 to 60,000 and from 60,000 to 80,000 resulted in a significant change in both the Nusselt number and friction factor.

4.2 Surrogate assisted optimization result

A surrogate-assisted optimization of the TOT heat exchanger was conducted. The statistical results of the optimum solutions are presented in Table 3, with the convergence history of all MHs shown in Figure 3. The hypervolume is computed and applied to statistical tests such as the average, standard deviation (Std), Best hypervolume value (Maximum), Worst hypervolume value (Minimum) and rank number of each model as presented. The results show that the MMIPDE is an outstanding algorithm for the design of the TOT heat exchanger, while the second best is RPBILDE, with average ranking numbers of 1.4545 and 1.5455 respectively. The MMIPDE presents the 6-winner prediction model, including RBF-linear, RBF-cubic spline, KNN-k=2, 3, 5 and 10, while other models are archived with RPBILDE. The third to last ranks are sorted as MOGWO, MOCS and NSGA-II with average ranks of 3.0909, 3.9091 and 5 respectively. Although the statistical results of the hypervolume from each prediction model cannot definitively determine which model gives the best result due to the presence of prediction errors, the optimum results obtained from the surrogate approximation must be evaluated for their actual function through CFD analyses. The percentage errors are computed and presented in Table 4. The optimum solutions, known as the Pareto front, from MMIPDE and RPBILDE from all prediction models, are selected as the sample population. Five selection points from each model are presented and the predicted fitness function, actual fitness function, percentage error for each representative population, and the average percentage error for each model are presented in Table 4. The fitness function is including Nusselt number (Nu) and the Poiseuille number (fRe). It can be seen that the RBF-Inverse Multiquadric with the MMIPDE algorithm provides acceptable predictions for both the Nusselt number and the Poiseuille number, with average errors of 20.9731 and 15.6011, respectively. On the other hand, the RPBILDE cannot find the most accurate model with a single approach. Two models that give the minimum error of the fitness function are the RBF-Inverse Multiquadric for the Nusselt number, value 18.3140, and the RBF-Inverse Quadric for the Poiseuille number, value 17.6819, respectively. The other models that are usable exhibit errors ranging from 21.8614 to 46.4616 for the Nusselt number, and from 19.0646 to 45.8472 for the Poiseuille number. However, the RBF – cubic spline model does not accept prediction results with errors of more than 100% for both Nusselt number and Poiseuille number.

The details of the sampling population of optimum solutions from MMIPDE and RPBILDE are presented in Table 5. The Nusselt number, friction factor, Nusselt number ratio (Nu_{ratio}), friction factor ratio (f_{ratio}), and thermal enhancement factor (TEF) are included. Therefore, the performance of the heat exchanger can be evaluated based on the thermal enhancement factor. It can be observed that the optimum solution from MMIPDE provides a thermal enhancement factor value between 0.7959 and 3.4262, with the maximum thermal enhancement factor computed from CFD data predicted by the KNN model with k=2. Meanwhile, for RPBILDE, the values are between 0.7959 and 3.4571, with the maximum thermal enhancement factor using optimum CFD data predicted by the RBF-Inverse Quadric model. It is evident that the most accurate prediction model does not necessarily provide the optimal solution. The maximum thermal enhancement factor did not originate from the most accurate predictor. This scenario is also known as the blessing and curse of uncertainty in surrogate-assisted optimization [30, 52].

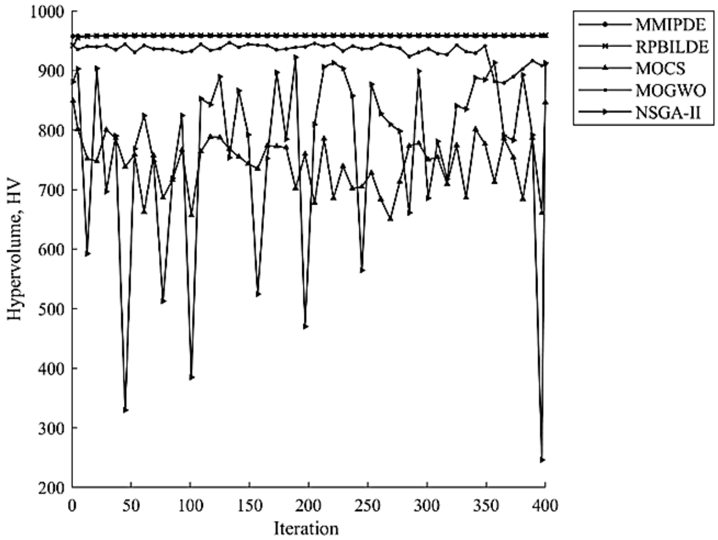

Figure 3 Convergence history of best run from MHs.

Table 3 Statistical results of optimum solutions for a twisted oval tube heat exchanger.

Prediction Model	Algorithm	MMIPDE	RPBILDE	MOCS	MOGWO	NSGA-II
KRG	Average	2,161.5383	**2,162.8051**	1,895.7890	2,085.6096	1,525.6109
	Std	7.7210	**13.4538**	77.5220	63.3562	560.7767
	Best (Maximum)	2,173.8360	**2,172.4594**	2,016.4463	2,131.6867	1,964.0729
	Worst (Minimum)	2,137.4763	**2,126.5933**	1,608.8110	1,765.3631	0.0923
	Rank no.	2	**1**	4	3	5
RBF-linear	Average	**2,193.4041**	2,189.2226	1,907.6113	2,148.8564	1,396.3344
	Std	**7.3240**	13.6899	74.0254	19.4459	671.2188
	Best (Maximum)	**2,200.2801**	2,199.4166	2,032.3161	2,177.1703	2,008.9788
	Worst (Minimum)	**2,170.2627**	2,151.3992	1,733.5163	2,099.4490	1.4061
	Rank no.	**1**	2	4	3	5
RBF-cubic spline	Average	**52,855,278.1746**	52,698,462.9735	48,199,107.8685	51,913,988.2815	35,384,887.6853
	Std	**15,177.2364**	40,746.0908	1,390,783.4748	434,357.6289	13,054,744.1876
	Best (Maximum)	**52,876,123.9492**	52,779,714.8047	50,144,656.2754	52,484,992.8965	50,594,278.0391
	Worst (Minimum)	**52,816,921.5391**	52,642,493.6836	45,166,052.4395	51,023,711.1592	2,112,868.2500
	Rank no.	**1**	2	4	3	5
RBF-Gaussian	Average	121.0361	**121.1530**	95.7549	110.5818	73.3476
	Std	0.0320	**0.0000**	6.2287	3.7242	34.4412
	Best (Maximum)	121.1128	**121.1530**	106.7589	114.6780	113.3430
	Worst (Minimum)	120.9813	**121.1530**	81.6520	97.4038	5.3853
	Rank no.	2	**1**	4	3	5

* The best algorithm for each model is presented in **bold**.

Table 3 Statistical results of optimum solutions for a twisted oval tube heat exchanger (continued).

Prediction Model	Algorithm	MMIPDE	RPBILDE	MOCS	MOGWO	NSGA-II
RBF-	Average	**52,855,278.1746**	52,698,462.9735	48,199,107.8685	51,913,988.2815	35,384,887.6853
RBF-	Average	846.9963	**847.5115**	663.7405	776.5637	490.4658
Multiquadric	Std	0.1580	**0.0003**	34.5933	30.9665	253.5948
	Best (Maximum)	847.3629	**847.5120**	724.5400	816.8924	764.1423
	Worst (Minimum)	846.7677	**847.5108**	585.5401	701.4754	0.0320
	Rank no.	2	**1**	4	3	5
RBF-Inverse Quadric	Average	946.1332	**946.4126**	738.0541	826.0281	744.0262
	Std	0.1908	**0.0000**	52.3473	27.2723	179.1498
	Best (Maximum)	946.4606	**946.4127**	849.4730	874.1095	890.4593
	Worst (Minimum)	945.7166	**946.4125**	614.6682	765.9834	0.0349
	Rank no.	2	**1**	4	3	5
RBF-Inverse Multiquadric	Average	958.1087	**958.7584**	743.8548	832.3830	739.5034
	Std	0.1883	**0.0000**	42.8002	56.5043	219.3364
	Best (Maximum)	958.4101	**958.7585**	846.4676	910.7008	912.6811
	Worst (Minimum)	957.5064	**958.7583**	640.6597	689.6823	0.0105
	Rank no.	2	**1**	4	3	5
KNN-k2	Average	**2,375.0312**	2,366.8752	2,035.6154	2,124.8462	2,083.9036
	Std	**0.2732**	10.2361	70.0487	80.5061	144.5610
	Best (Maximum)	**2,375.1208**	2,375.0483	2,087.3303	2,262.5570	2,258.2292
	Worst (Minimum)	**2,374.2253**	2,339.6181	1,847.0471	1,937.3501	1,723.5483
	Rank no.	**1**	2	4	3	5
KNN-k3	Average	**2,083.5933**	2,071.3691	1,821.0007	1,821.9030	1,856.5623
	Std	**1.0362**	9.3166	75.3619	62.3043	96.4820
	Best (Maximum)	**2,084.8318**	2,081.8523	2,011.2253	1,940.7358	1,972.1425
	Worst (Minimum)	**2,079.3359**	2,042.5067	1,705.0651	1,676.7944	1,623.7411
	Rank no.	**1**	2	4	3	5
KNN-k5	Average	**1,816.9582**	1,804.5440	1,638.1167	1,729.0349	1,578.6385
	Std	**2.5980**	9.5592	58.3791	36.3950	100.4449
	Best (Maximum)	**1,819.6460**	1,815.2492	1,772.0307	1,766.7217	1,685.8615
	Worst (Minimum)	**1,807.1827**	1,783.1673	1,504.2447	1,630.8056	1,255.6750
	Rank no.	**1**	2	4	3	5
KNN-k10	Average	**1,513.4839**	1,447.6887	1,434.8322	1,352.5270	1,243.6759
	Std	**1.9708**	38.8020	44.1670	83.1579	118.3504
	Best (Maximum)	**1,515.5378**	1,512.4316	1,505.9406	1,456.8178	1,353.7882
	Worst (Minimum)	**1,506.9289**	1,399.4119	1,339.4072	1,019.9855	832.1377
	Rank no.	**1**	2	3	4	5
	Average Rank	**1.4545**	1.5455	3.9091	3.0909	5

* The best algorithm for each model is presented in **bold**.

Table 4 Comparison of surrogate model results and CFD results of MMIPDE and RPBILDE.

Prediction model	MMIPDE									RPBILDE								
	Pareto point no.	$f_{prediction}$		f_{actual}		% Error		Avg. Error [%]		Pareto point no.	$f_{prediction}$		f_{actual}		% Error		Avg. Error [%]	
		Nu	*fRe*	*Nu*	*fRe*	*Nu*	*fRe*	*Nu*	*fRe*		*Nu*	*fRe*	*Nu*	*fRe*	*Nu*	*fRe*	*Nu*	*fRe*
KRG	1	3.9329	62.9632	4.3084	78.8142	8.7158	20.1118			1	4.0749	71.0841	4.2554	77.9868	4.2409	8.8511		
	3	5.5846	77.6355	7.9514	131.6594	29.7650	41.0331			5	5.7769	85.9757	7.9853	137.2684	27.6556	37.3668		
	6	7.1993	97.9516	12.3371	195.7667	41.6454	49.9651	32.3597	36.2471	8	7.1260	96.2031	13.0163	201.4324	45.2533	52.2405	31.9747	34.2509
	8	8.3088	111.0474	16.9079	249.5852	50.8583	55.5072			11	8.1491	107.1185	16.9079	249.5852	51.8031	57.0814		
	49	15.0642	345.9319	21.7734	405.1579	30.8138	14.6180			46	15.0409	341.4889	21.7734	405.1579	30.9208	15.7146		
RBF linear	1	4.0520	69.6566	4.2832	78.1107	5.3985	10.8233			1	4.0520	69.6566	4.2832	78.1107	5.3985	10.8233		
	2	5.6267	83.3440	7.7971	129.1014	27.8362	35.4430			4	5.6783	85.2989	8.0251	132.0851	29.2427	35.4213		
	4	6.9215	95.5402	12.5610	194.8669	44.8973	50.9715	32.7643	33.3791	9	7.1922	103.9784	12.6967	196.7953	43.3536	47.1642	32.6907	32.5458
	6	7.8917	107.0646	17.2550	249.9400	54.2645	57.1639			11	7.9314	107.8949	17.2550	249.9400	54.0340	56.8317		
	50	14.7939	366.6418	21.5733	418.9888	31.4250	12.4936			48	14.7939	366.6619	21.5733	418.9888	31.4248	12.4889		
RBF cubic spline	1	-8929.9531	-10112.7500	11.7592	195.8403	76040.3353	5263.7751			1	-8656.1563	-10005.2500	12.7665	203.9469	67903.5694	5005.8107		
	38	-2421.1406	-3301.5000	13.1187	259.1499	18555.6304	1373.9732			34	-2421.1406	-3301.5000	13.1187	259.1499	18555.6304	1373.9732		
	40	-1944.1250	-2636.7500	13.7632	269.0811	14225.5099	1079.9089	24,578.47	1,814.08	36	-1944.1094	-2640.2500	13.7632	269.0811	14225.3963	1081.2097	22,951.19	1,762.73
	41	-1469.9844	-2165.6250	10.5405	174.9437	14046.0063	1337.8980			37	-1469.9688	-2165.5000	10.5405	174.9437	14045.8581	1337.8265		
	50	15.8125	346.0000	21.0601	406.4756	24.9174	14.8780			46	15.6875	346.0000	21.0601	406.4756	25.5109	14.8780		
RBF Gaussian	1	6.5696	138.5821	4.1204	83.4986	59.4417	65.9693			1	6.5696	138.5821	4.0726	83.6281	61.3128	65.7123		
	16	7.6346	162.4795	10.1891	164.5031	25.0706	1.2301			29	8.4472	181.1325	13.9120	300.3938	39.2811	39.7016		
	33	8.8162	189.6664	14.5769	263.6302	39.5193	28.0559	45.3049	34.6362	33	8.7137	187.2958	14.3334	317.9030	39.2070	41.0840	46.4617	45.8472
	39	9.2243	199.1197	17.4446	290.6791	47.1221	31.4984			37	8.9802	193.4594	15.1748	308.7692	40.8214	37.3450		
	49	9.7850	212.1660	21.9250	396.0337	55.3708	46.4273			50	9.8423	213.5004	20.3716	390.9783	51.6861	45.3933		
RBF Multiquadric	1	3.9443	80.7158	4.2832	78.1107	7.9135	3.3352			1	3.9443	80.7158	4.2832	78.1107	7.9135	3.3352		
	6	4.9677	100.9121	6.7709	147.4934	26.6316	31.5820			8	5.2394	106.5754	7.1991	155.5386	27.2218	31.4797		
	10	5.7296	117.0485	7.9660	134.7803	28.0741	13.1561	21.8614	19.7690	10	5.6218	114.7160	7.7941	128.9217	27.8708	11.0189	23.4102	19.0647
	12	6.1484	126.2880	8.7189	145.9466	29.4820	13.4697			26	8.4114	179.2086	13.3175	204.0806	36.8390	12.1873		
	50	12.5450	276.5988	15.1520	441.1625	17.2059	37.3023			50	12.5450	276.5988	15.1520	441.1625	17.2059	37.3023		
RBF Inverse Quadric	1	3.9065	79.9194	3.3312	95.7131	17.2711	16.5011			1	3.9065	79.9194	3.3312	95.7131	17.2711	16.5011		
	13	6.3011	130.9722	7.2579	203.1487	13.1831	35.5289			24	8.2841	175.8331	9.1058	258.2197	9.0233	31.9056		
	35	10.1996	221.0120	12.6131	306.2610	19.1350	27.8354	24.6146	22.7284	36	10.4829	227.4547	12.0431	344.9035	12.9552	34.0526	23.2411	**17.6819**
	45	12.0082	264.0171	19.9880	280.4253	39.9228	5.8512			46	12.2402	269.2806	19.9880	277.4100	38.7623	2.9305		
	49	12.8382	282.8552	19.3232	392.4465	33.5608	27.9252			50	13.0352	287.4426	21.0905	296.3931	38.1937	3.0198		

Table 4 Comparison of surrogate model results and CFD results of MMIPDE and RPBILDE (continued).

Prediction model	MMIPDE									RPBILDE								
	Pareto point no.	$f_{prediction}$		f_{actual}		% Error		Avg. Error [%]		Pareto point no.	$f_{prediction}$		f_{actual}		% Error		Avg. Error [%]	
		Nu	*fRe*	*Nu*	*fRe*	*Nu*	*fRe*	*Nu*	*fRe*		*Nu*	*fRe*	*Nu*	*fRe*	*Nu*	*fRe*	*Nu*	*fRe*
RBF	1	3.8236	78.2007	3.3312	95.7131	14.7833	18.2968			1	3.8236	78.2007	3.3312	95.7131	14.7833	18.2968		
Inverse	21	7.7003	162.3470	8.4144	234.1746	8.4868	30.6727			27	8.7539	187.3376	10.0814	286.6694	13.1680	34.6503		
Multiquadric	37	10.7365	233.5484	13.5661	278.8054	20.8578	16.2324	**20.9731**	**15.6011**	38	10.7857	234.7090	12.5362	359.7790	13.9638	34.7630	**18.3140**	24.5892
	43	11.7755	258.0665	18.1829	285.3975	35.2389	9.5765			43	11.7089	256.5104	13.5662	391.3039	13.6905	34.4473		
	49	12.7843	281.5354	17.1598	272.7336	25.4986	3.2273			50	12.9877	286.4277	20.2819	288.7046	35.9643	0.7886		
KNN	1	4.0533	69.7147	4.6193	83.2721	12.2536	16.2809			1	4.0533	69.7147	5.8016	99.8775	30.1343	30.1998		
k = 2	17	8.3305	113.0126	19.2386	271.4552	56.6990	58.3679			13	7.9771	109.2842	17.9513	256.1228	55.5627	57.3313		
	34	11.5639	192.4547	21.5085	322.9322	46.2357	40.4040	34.4429	28.4331	26	11.5639	192.4547	21.4454	330.8093	46.0777	41.8231	36.2279	28.9890
	43	13.5351	287.1961	19.0126	355.2486	28.8098	19.1563			37	13.5351	287.1961	17.4760	321.5596	22.5502	10.6865		
	50	14.7051	385.6607	20.4853	418.9992	28.2164	7.9567			46	14.7051	385.6607	20.0930	405.5507	26.8146	4.9044		
KNN	1	4.0522	70.4475	5.7626	99.2234	29.6812	29.0011			1	4.0522	70.4475	4.2447	77.9023	4.5347	9.5694		
k = 3	6	6.1250	91.8576	9.8706	161.4379	37.9472	43.1003			7	6.0541	87.5929	10.2343	163.4639	40.8451	46.4145		
	27	10.8161	170.8323	18.6348	283.9936	41.9577	39.8464	33.2286	27.2504	25	10.8161	170.8323	19.5957	295.5244	44.8038	42.1935	28.3518	24.0099
	47	14.2808	316.0215	20.0958	356.6531	28.9365	11.3925			44	14.1850	303.2131	20.0190	375.9356	29.1424	19.3444		
	50	14.5432	358.6213	20.0930	411.7899	27.6203	12.9116			48	14.5432	358.6213	18.7492	367.9201	22.4327	2.5274		
KNN	1	4.0345	71.7083	4.3308	79.5789	6.8426	9.8903			1	4.0345	71.7083	5.5244	98.1982	26.9701	26.9760		
k = 5	9	6.3492	96.3277	10.3174	168.9336	38.4611	42.9790			8	6.3797	98.0392	10.2757	168.6679	37.9146	41.8744		
	17	8.6622	122.9959	19.6207	273.1486	55.8517	54.9711	34.7660	31.5745	15	8.6622	122.9959	19.6207	273.1486	55.8517	54.9711	36.9825	32.0011
	36	12.2751	221.5955	21.0400	318.2973	41.6586	30.3810			33	12.3266	235.9314	20.2578	327.8868	39.1513	28.0448		
	50	14.2488	336.6602	20.6552	418.9992	31.0159	19.6514			46	14.2488	336.6602	19.0047	366.4895	25.0247	8.1392		
KNN	1	3.9780	74.3625	5.8320	100.6495	31.7902	26.1173			1	3.9780	74.3625	5.8127	102.8220	31.5643	27.6784		
k = 10	4	4.9274	89.0521	5.8268	111.0711	15.4343	19.8242			4	4.9191	86.0450	5.8268	111.0711	15.5780	22.5316		
	10	6.7372	111.1972	10.4197	165.3537	35.3412	32.7519	30.8816	28.1206	10	6.6108	104.6799	10.4197	165.3537	36.5549	36.6934	31.4900	31.1409
	16	8.4142	135.0902	14.4545	234.5516	41.7881	42.4049			17	8.4142	135.0902	14.4545	234.5516	41.7881	42.4049		
	50	13.4390	316.3245	19.2134	392.9721	30.0541	19.5046			47	13.2677	283.2568	19.5012	384.8404	31.9645	26.3963		

* The minimum value is presented in **bold**.

Table 5 CFD detailed results of optimum solution from MMIPDE and RPBILDE.

Prediction model	MMIPDE						RPBILDE					
	Pareto point no.	*Nu*	*f*	*Nu* ratio	*f* ratio	*TEF*	Pareto point no.	*Nu*	*f*	*Nu* ratio	*f* ratio	*TEF*
KRG	1	4.3084	0.7881	1.1772	1.2315	1.0982	1	4.2554	0.7799	1.1627	1.2185	1.0885
	3	7.9514	0.2633	2.1725	2.0572	1.7082	5	7.9853	0.2745	2.1818	2.1448	1.6918
	6	12.3371	0.1958	3.3708	3.0589	2.3221	8	13.0163	0.2014	3.5564	3.1474	2.4267
	8	16.9079	0.1664	4.6196	3.8998	2.9349	11	16.9079	0.1664	4.6196	3.8998	2.9349
	49	21.7734	0.2026	5.9490	6.3306	3.2159	46	21.7734	0.2026	5.9490	6.3306	3.2159
RBF linear	1	4.2832	0.7811	1.1703	1.2205	1.0951	1	4.2832	0.7811	1.1703	1.2205	1.0951
	2	7.7971	0.2582	2.1304	2.0172	1.6861	4	8.0251	0.2642	2.1926	2.0638	1.7222
	4	12.5610	0.1949	3.4320	3.0448	2.3679	9	12.6967	0.1968	3.4690	3.0749	2.3856
	6	17.2550	0.1666	4.7145	3.9053	2.9938	11	17.2550	0.1666	4.7145	3.9053	2.9938
	50	21.5733	0.2095	5.8943	6.5467	3.1508	48	21.5733	0.2095	5.8943	6.5467	3.1508
RBF cubic spline	1	11.7592	0.1567	3.2129	3.0600	2.2130	1	12.7665	0.1658	3.4881	3.1867	2.3703
	38	13.1187	0.2468	3.5843	4.0492	2.2488	34	13.1187	0.2468	3.5843	4.0492	2.2488
	40	13.7632	0.2587	3.7604	4.2044	2.3299	36	13.7632	0.2587	3.7604	4.2044	2.3299
	41	10.5405	0.1698	2.8799	2.7335	2.0597	37	10.5405	0.1698	2.8799	2.7335	2.0597
	50	21.0601	0.2032	5.7541	6.3512	3.1071	46	21.0601	0.2032	5.7541	6.3512	3.1071
RBF Gaussian	1	4.1204	0.8350	1.1258	1.3047	1.0303	1	4.0726	0.8363	1.1127	1.3067	1.0178
	16	10.1891	0.2136	2.7839	2.5704	2.0323	29	13.9120	0.2567	3.8011	4.6937	2.2702
	33	14.5769	0.1953	3.9828	4.1192	2.4845	33	14.3334	0.2445	3.9162	4.9672	2.2952
	39	17.4446	0.1851	4.7663	4.5419	2.8781	37	15.1748	0.2159	4.1461	4.8245	2.4537
	49	21.9250	0.2021	5.9904	6.1880	3.2629	50	20.3716	0.1955	5.5660	6.1090	3.0448
RBF Multiquadric	1	4.2832	0.7811	1.1703	1.2205	1.0951	1	4.2832	0.7811	1.1703	1.2205	1.0951
	6	6.7709	0.3881	1.8500	2.3046	1.4006	8	7.1991	0.3617	1.9670	2.4303	1.4630
	10	7.9660	0.2592	2.1765	2.1059	1.6980	10	7.7941	0.2578	2.1295	2.0144	1.6862
	12	8.7189	0.2432	2.3822	2.2804	1.8099	26	13.3175	0.1890	3.6387	3.1888	2.4721
	50	15.1520	0.2206	4.1399	6.8932	2.1753	50	15.1520	0.2206	4.1399	6.8932	2.1753
RBF Inverse Quadric	1	3.3312	0.9571	0.9102	1.4955	0.7959	1	3.3312	0.9571	0.9102	1.4955	0.7959
	13	7.2579	0.2783	1.9830	3.1742	1.3493	24	9.1058	0.2532	2.4879	4.0347	1.5628
	35	12.6131	0.2127	3.4462	4.7853	2.0451	36	12.0431	0.2330	3.2905	5.3891	1.8768
	45	19.9880	0.1524	5.4612	4.3816	3.3374	46	19.9880	0.1491	5.4612	4.3345	3.3495
	49	19.3232	0.2044	5.2795	6.1320	2.8845	50	21.0905	0.1505	5.7624	4.6311	3.4571

Table 5 CFD detailed results of optimum solution from MMIPDE and RPBILDE (continued).

Prediction model	MMIPDE						RPBILDE					
	Pareto point no.	*Nu*	*f*	*Nu* ratio	*f* ratio	*TEF*	Pareto point no.	*Nu*	*f*	*Nu* ratio	*f* ratio	*TEF*
RBF	1	3.3312	0.9571	0.9102	1.4955	0.7959	1	3.3312	0.9571	0.9102	1.4955	0.7959
Inverse	21	8.4144	0.2573	2.2990	3.6590	1.4920	27	10.0814	0.2450	2.7545	4.4792	1.6710
Multiquadric	37	13.5661	0.1799	3.7066	4.3563	2.2695	38	12.5362	0.2306	3.4252	5.6215	1.9263
	43	18.1829	0.1640	4.9680	4.4593	3.0183	43	13.5662	0.2262	3.7066	6.1141	2.0271
	49	17.1598	0.1443	4.6885	4.2615	2.8919	50	20.2819	0.1473	5.5415	4.5110	3.3538
KNN	1	4.6193	0.5551	1.2621	1.3011	1.1561	1	5.8016	0.3699	1.5851	1.5606	1.3666
k = 2	17	19.2386	0.1551	5.2565	4.2415	3.2473	13	17.9513	0.1652	4.9047	4.0019	3.0893
	34	21.5085	0.1615	5.8766	5.0458	3.4262	26	21.4454	0.1688	5.8594	5.1689	3.3889
	43	19.0126	0.1785	5.1947	5.5508	2.9339	37	17.4760	0.1827	4.7749	5.0244	2.7878
	50	20.4853	0.2095	5.5971	6.5469	2.9919	46	20.0930	0.2048	5.4899	6.3367	2.9667
KNN	1	5.7626	0.3675	1.5745	1.5504	1.3604	1	4.2447	0.7790	1.1597	1.2172	1.0862
k = 3	6	9.8706	0.2153	2.6969	2.5225	1.9812	7	10.2343	0.2180	2.7962	2.5541	2.0456
	27	18.6348	0.1595	5.0915	4.4374	3.0984	25	19.5957	0.1642	5.3540	4.6176	3.2152
	47	20.0958	0.1960	5.4907	5.5727	3.0970	44	20.0190	0.1889	5.4697	5.8740	3.0315
	50	20.0930	0.2112	5.4899	6.4342	2.9516	48	18.7492	0.2079	5.1227	5.7488	2.8596
KNN	1	4.3308	0.7234	1.1833	1.2434	1.1004	1	5.5244	0.3928	1.5094	1.5343	1.3087
k = 5	9	10.3174	0.2252	2.8190	2.6396	2.0398	8	10.2757	0.2249	2.8076	2.6354	2.0326
	17	19.6207	0.1561	5.3608	4.2679	3.3049	15	19.6207	0.1561	5.3608	4.2679	3.3049
	36	21.0400	0.1624	5.7486	4.9734	3.3678	33	20.2578	0.1664	5.5349	5.1232	3.2107
	50	20.6552	0.2095	5.6435	6.5469	3.0167	46	19.0047	0.2059	5.1925	5.7264	2.9024
KNN	1	5.8320	0.3471	1.5934	1.5726	1.3702	1	5.8127	0.3546	1.5882	1.6066	1.3560
k = 10	4	5.8268	0.3702	1.5920	1.7355	1.3248	4	5.8268	0.3702	1.5920	1.7355	1.3248
	10	10.4197	0.2205	2.8469	2.5837	2.0747	10	10.4197	0.2205	2.8469	2.5837	2.0747
	16	14.4545	0.1876	3.9493	3.6649	2.5615	17	14.4545	0.1876	3.9493	3.6649	2.5615
	50	19.2134	0.1995	5.2496	6.1402	2.8668	47	19.5012	0.2162	5.3282	6.0131	2.9301

The average ranking of the hypervolume statistical test is shown in Table 3, and the percentage error data of the fitness function in Table 4. As discussed earlier, the RBF-Inverse Multiquadric model with the MMIPDE algorithm offers satisfactory predictions for both the Nusselt number and the Poiseuille number. The sampling points of the Pareto front from the RBF-Inverse Multiquadric model with the MMIPDE algorithm is illustrated in Figure 4.

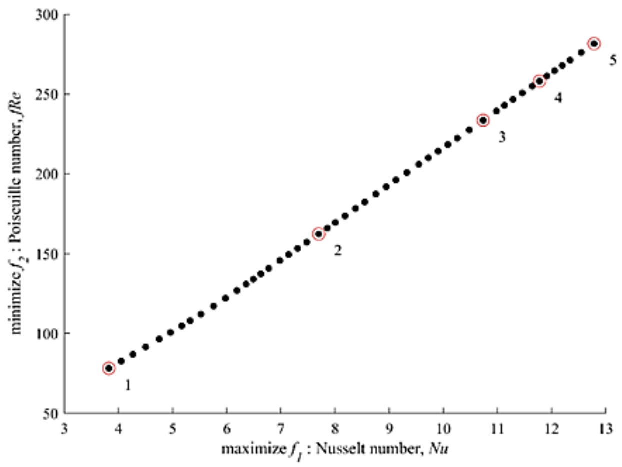

Figure 4 Pareto front of best run from MMIPDE and selected sampling solution.

All five optimal models are illustrated in Figure 5 (a)**.** The fluid temperature field and 2D flow structure (in the form of a vector) on the transverse plane is depicted in Figure 5 (b)**.** It is indicated that the twisted oval tube creates a swirl flow leading to disruption of the boundary layer around the tube wall, enhancing the heat transfer on the tube wall as presented in Figure 5 (c)**.** It is visible that the case III showed the highest heat transfer on the wall.

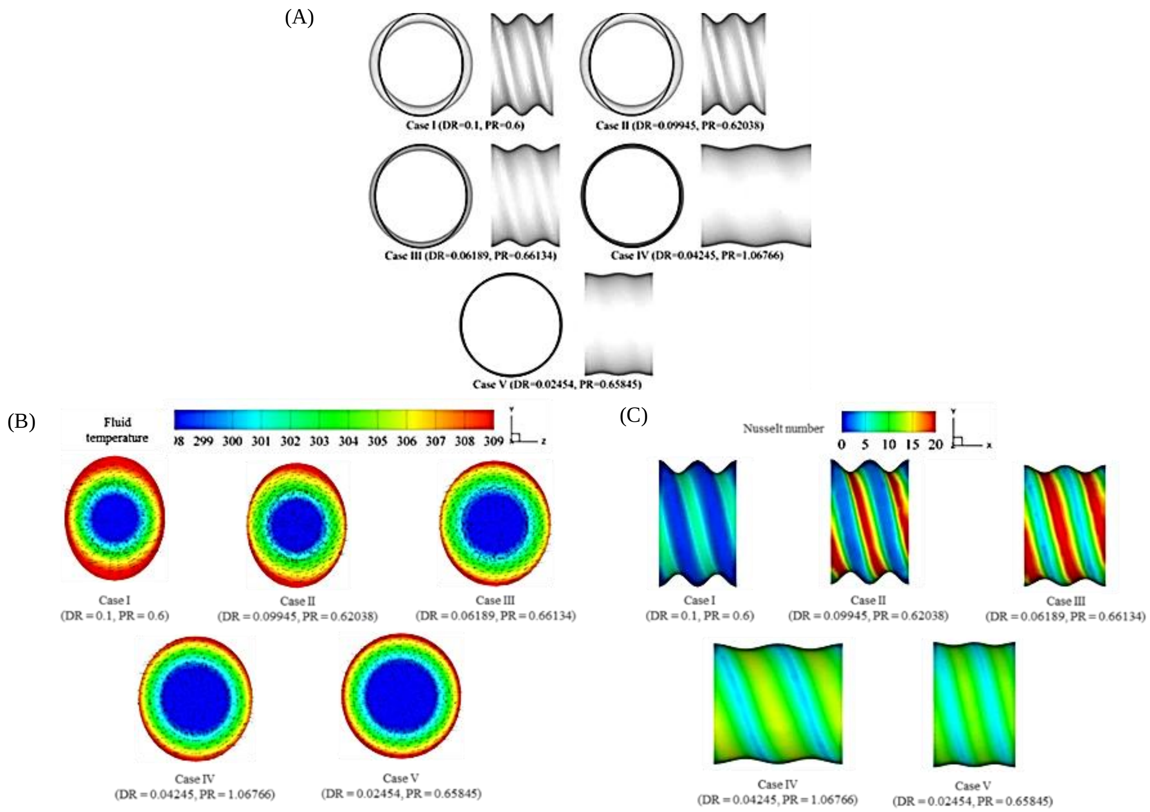

Figure 5 (A) The optimum geometry model from MMIPDE, (B) Temperature distribution and flow direction profile in cross-sectional area, and (C) The Nusselt number profile at wall surface of optimum solution from MMIPDE.

5. Conclusion

Improving the twisted oval tube (TOT) design is proposed. Surrogate assisted design optimization was applied. The geometric parameters for 125 cases of TOT with five various pitch to diameter ratios (PR = p/D = 0.6, 0.8, 1.0, 1.2, and 1.4), cross-sectional ratios (DR = a/b = 0.02, 0.04, 0.06, 0.08, and 0.10) and (*Re* = 100, 500, 1,000, 1,500 and 2,000) were examined. The eleven surrogate models including one Kriging model (KRG), six radial basis functions (RBF), the kernel including linear kernel, cubic spline kernel, Gaussian kernel, multiquadric kernel, inverse quadric kernel, inverse multiquadric kernel, and four K-nearest neighborhood method (K-NN); the kernels including k = 2, 3, 5 and 10 were investigated. Five metaheuristics; multi-objective meta-heuristic with iterative parameter distribution estimation (MMIPDE), hybrid real-code population-based incremental learning and differential evolution (RPBILDE), and multi-objective cuckoo Search (MOCS), multi-objective grey wolf optimizer (MOGWO), non-dominated sorting genetic algorithm II (NSGA-II) were compared. The key findings of this article can be summarized as follows.

1. A total of 125 cases were selected for training data. All surrogate models were constructed using the training data and the optimum solution found, called the Pareto front. The results found all surrogate models are acceptable predictions with percentage error between 15.6011 and 46.4617, except for the RBF – cubic spline; this model gives an error of more than 100% for all predictions.
2. Based on the comparisons of the statistical tests and error prediction models in Tables 4 and Table 5, the best prediction model is the RBF-Inverse Multiquadric with the MMIPDE algorithm. It provides acceptable predictions for both the Nusselt number and the Poiseuille number, with average errors of 20.9731 and 15.6011, respectively.
3 Investigating the best solution, based on the most accurate prediction model, the RBF-Inverse Multiquadric with the MMIPDE, the optimum geometry model, heat transfer, and friction factor characteristics of the sample optimum solution are illustrated in Figures 5, respectively. The percentage errors were computed, and it was found that the Poiseuille number was more accurate than the Nusselt number. This shows that the surrogate model can only capture the trend of heat transfer and friction factor behavior of the twisted oval tube. Therefore, this powerful prediction method can be further improved in the future.

This research provides a base line to set the research direction for the design of twisted oval tube heat exchangers. Following the results, the surrogate model will be improved. Many topics can be further studied, for example, the geometry parameter, the governing equation can be a turbulent model, or a new optimization procedure can be presented.

6. Acknowledgements

This Research was Financially Supported by the Faculty of Engineering, Mahasarakham University, (Grant No. L-06/2566).

7. References

[1] Eiamsa-ard S, Chuwattanakul V, Safikhani H, et al. Prediction of heat transfer and fluid flow in a cross-corrugated tube using numerical methods, artificial neural networks and genetic algorithms. Thermophys Aeromechanics 2022; 29: 229–247.
[2] Samadifar M, Toghraie D. Numerical simulation of heat transfer enhancement in a plate-fin heat exchanger using a new type of vortex generator. Appl Therm Eng. 2018; 133: 671–681.
[3] Wansasueb K, Pholdee N, Bureerat S. Optimum radii and heights of U-shaped baffles in a square duct heat exchanger using surrogate-assisted optimization. Eng Appl Sci Res. 2017; 44: 84–89.
[4] Tharakeshwar TK, Seetharamu KN, Durga Prasad B. Multi-objective optimization using bat algorithm for shell and tube heat exchangers. Appl Therm Eng. 2017; 110: 1029–1038.
[5] Bureerat S, Srisomporn S. Optimum plate-fin heat sinks by using a multi-objective evolutionary algorithm. Eng Optim. 2010; 42: 305–323.
[6] Augspurger M, Choi KK, Udaykumar HS. Optimizing fin design for a PCM-based thermal storage device using dynamic Kriging. Int J Heat Mass Transf. 2018; 121: 290–308.
[7] Promthaisong P, Chuwattanakul V, Eiamsa-Ard S. Thermal and swirl flow topologies in a twisted square duct with a multi-twisted tape installed. J Therm Sci Technol. 2020; 15: JTST0008–JTST0008.

[8] Promthaisong P, Jedsadaratanachai W, Eiamsa-Ard S. 3D Numerical study on the flow topology and heat transfer characteristics of turbulent forced convection in spirally corrugated tube. Numer Heat Transf Part A Appl. 2016; 69: 607–629.

[9] Hosseinnezhad R, Akbari OA, Hassanzadeh Afrouzi H, et al. Numerical study of turbulent nanofluid heat transfer in a tubular heat exchanger with twin twisted-tape inserts. J Therm Anal Calorim. 2018; 132: 741–759.

[10] Samutpraphut B, Eiamsa-ard S, Chuwattanakul V, et al. Influence of sawtooth twisted tape on thermal enhancement of heat exchanger tube. Energy Report.s 2023; 9: 696–703.

[11] Miansari M, Valipour MA, Arasteh H, et al. Energy and exergy analysis and optimization of helically grooved shell and tube heat exchangers by using Taguchi experimental design. J Therm Anal Calorim. 2020; 139: 3151–3164.

[12] Han JC, Glicksman LR, Rohsenow WM. An investigation of heat transfer and friction for rib-roughened surfaces. Int J Heat Mass Transf. 1978; 21: 1143–1156.

[13] Thianpong C, Eiamsa-Ard P, Eiamsa-Ard S. Heat transfer and thermal performance characteristics of heat exchanger tube fitted with perforated twisted-tapes. Heat Mass Transf und Stoffuebertragung. 2012; 48: 881–892.

[14] Maakala V, Järvinen M, Vuorinen V. Optimizing the heat transfer performance of the recovery boiler superheaters using simulated annealing, surrogate modeling, and computational fluid dynamics. Energy. 2018; 160: 361–377.

[15] Naphon P, Wiriyasart S. Experimental study on laminar pulsating flow and heat transfer of nanofluids in micro-fins tube with magnetic fields. Int J Heat Mass Transf. 2018; 118: 297–303.

[16] Lu J, Sheng X, Ding J, et al. Transition and turbulent convective heat transfer of molten salt in spirally grooved tube. Exp Therm Fluid Sci. 2013; 47: 180–185.

[17] Pour Razzaghi MJ, Ghassabian M, Daemiashkezari M, et al. Thermo-hydraulic performance evaluation of turbulent flow and heat transfer in a twisted flat tube: A CFD approach. Case Stud Therm Eng. 2022; 35: 102107.

[18] Promthaisong P, Chuwattanakul V, Eiamsa-ard S. 3D numerical analysis of thermal-hydraulic behaviors of turbulent flow inside twisted square ducts. Thermophys Aeromechanics 2020; 27: 345–357.

[19] Eiamsa-ard S, Maruyama N, Hirota M, et al. Heat transfer mechanism in ribbed twisted-oval tubes. Int J Therm Sci. 2023; 193: 108532.

[20] Daniali OA, Toghraie D, Eftekhari SA. Thermo-hydraulic and economic optimization of Iranol refinery oil heat exchanger with Copper oxide nanoparticles using MOMBO. Phys A Stat Mech its Appl. 2020; 540: 123010.

[21] Moradi A, Toghraie D, Isfahani AHM, et al. An experimental study on MWCNT–water nanofluids flow and heat transfer in double-pipe heat exchanger using porous media. J Therm Anal Calorim. 2019; 137: 1797–1807.

[22] Hemmat Esfe M, Hajmohammad H, Toghraie D, et al. Multi-objective optimization of nanofluid flow in double tube heat exchangers for applications in energy systems. Energy. 2017; 137: 160–171.

[23] Patankar S V., Spalding DB. Heat Mass Transf Bound Layers. 1970; 1970.

[24] Patankar S V., Spalding DB. A calculation procedure for heat, mass and momentum transfer in three-dimensional parabolic flows. Int J Heat Mass Transf. 1972; 15: 1787–1806.

[25] Knecht S, Zdravkov D, Albers A. Surrogate models for heat transfer in oscillating flow with a local heat source. Fluids 2023; 8(3):80.

[26] Briceno-Mena LA, Arges CG, Romagnoli JA. Machine learning-based surrogate models and transfer learning for derivative free optimization of HT-PEM fuel cells. Comput Chem Eng. 2023; 171: 108159.

[27] Zamengo M, Wu S, Yoshida R, et al. Multi-objective optimization for assisting the design of fixed-type packed bed reactors for chemical heat storage. Appl Therm Eng. 2023; 218: 119327.

[28] Fawaz A, Hua Y, Le Corre S, et al. Topology optimization of heat exchangers: A review. Energy. 2022; 252: 124053.

[29] Wansasueb K, Bureerat S. Design of turbulators for a rectangular duct heat exchanger. In: Phadungsak Rattanadecho (ed) The 29th Conference of Mechanical Engineering Network of Thailand. Nakhon Ratchasima: Thai Society of Mechanical Engineers, 2015;529–536.

[30] Wansaseub K, Pholdee N, Bureerat S. Optimal U-shaped baffle square-duct heat exchanger through surrogate-assisted self-adaptive differential evolution with neighbourhood search and weighted exploitation-exploration. Appl Therm Eng. 2017; 118: 455–463.

[31] Eiamsa-ard S, Promthaisong P, Thianpong C, et al. Influence of three-start spirally twisted tube combined with triple-channel twisted tape insert on heat transfer enhancement. Chem Eng Process Process Intensif. 2016; 102: 117–129.

[32] Forrester AIJ, Sóbester A, Keane AJ. Engineering Design via Surrogate Modelling. Wiley, 2008. Epub ahead of print July 2008.

[33] Forrester AIJ, Sóbester A, Keane AJ. Engineering design via surrogate modelling : A practical guide. J Wiley, 2008.
[34] Ghosh J, Nag A. An overview of radial basis function networks. Physica, Heidelberg, pp. 1–36.
[35] Zhang Z. Introduction to machine learning: K-nearest neighbors. Ann Transl Med; 4. Epub ahead of print 1 June 2016. DOI: 10.21037/atm.2016.03.37.
[36] Gan G, Valdez EA. Ordinary kriging. Metamodeling Var Annu 2019; 69–94.
[37] Panagant N, Bureerat S. Truss topology, shape and sizing optimization by fully stressed design based on hybrid grey wolf optimization and adaptive differential evolution. Eng Optim 2018; 50: 1645–1661.
[38] Wu Y, Wang H, Zhang B, et al. Using radial basis function networks for function approximation and classification. ISRN Appl Math. 2012; 2012: 1–34.
[39] Schaback R. Radial basis functions viewed from cubic splines. In: Multivariate Approximation and Splines. Birkhäuser Basel, pp. 245–258.
[40] Javaran SH, Khaji N. Inverse multiquadric (IMQ) function as radial basis function for plane dynamic analysis using dual reciprocity boundary element method. Tarbiat Modares University. 2012.
[41] Parzlivand F, Shahrezaee A. The use of inverse quadratic radial basis functions for the solution of an inverse heat problem. Bull Iran Math Soc. 2016;42(5):1127-42.
[42] Sarra SA. Integrated multiquadric radial basis function approximation methods. Comput Math with Appl. 2006; 51: 1283–1296.
[43] Tada T, Hitomi K, Wu Y, et al. K-mean clustering algorithm for processing signals from compound semiconductor detectors. Nucl Instrum Methods Phys Res Sect A. 2011; 659: 242–246.
[44] Ahmad A, Dey L. A k-mean clustering algorithm for mixed numeric and categorical data. Data Knowl Eng 2007; 63: 503–527.
[45] Wansasueb K, Pholdee N, Panagant N, et al. Multiobjective meta-heuristic with iterative parameter distribution estimation for aeroelastic design of an aircraft wing. Eng Comput. 2020; 1–19.
[46] Pholdee N, Bureerat S. Hybridisation of real-code population-based incremental learning and differential evolution for multiobjective design of trusses. Inf Sci (Ny) 2013; 223: 136–152.
[47] Yang XS, Deb S. Multiobjective cuckoo search for design optimization. Comput Oper Res. 2013; 40: 1616–1624.
[48] Mirjalili SM, Saremi S, Mirjalili SM, et al. Multi-objective grey wolf optimizer: A novel algorithm for multi-criterion optimization. Expert Syst Appl. 2016; 47: 106–119.
[49] Campos Ciro G, Dugardin F, Yalaoui F, et al. A NSGA-II and NSGA-III comparison for solving an open shop scheduling problem with resource constraints. IFAC-PapersOnLine. 2016; 49: 1272–1277.
[50] Zitzler E. Evolutionary algorithms for multiobjective optimization. Shaker. Epub ahead of print 1999.
[51] Inropera FP, DeWitt DP. Introduction to Heat Transfer. 5th ed. 2006.
[52] Pholdee N, Baek HM, Bureerat S, et al. Process optimization of a non-circular drawing sequence based on multi-surrogate assisted meta-heuristic algorithms. J Mech Sci Technol. 2015; 29: 3427–3436.